JOURNAL OF GEOPHYSICAL RESEARCH, VOL. 115, B07408, doi:10.1029/2009JB006572, 2010

Displacement field in contraction-driven faults

Hosung Shin,[1] J. Carlos Santamarina,[2] and Joseph A. Cartwright[3]

Received 27 April 2009; revised 7 January 2010; accepted 4 March 2010; published 20 July 2010.

[1] We investigate the distribution of strain and deformation in the host sediment that arises once a contraction-driven shear fault has localized and propagated under a zero-lateral strain condition. Numerical modeling of displacement distributions compares well with those measured using 3D seismic data. The parameters that determine the displacement field for a single normal fault embedded in sediments are fault height, overburden effective stress, stiffness, and residual friction angle (or post-peak strength). Proximity to the free boundary biases the displacement pattern, which becomes asymmetric. Although the measured displacements and numerical predictions are similar, the measured magnitude requires pronounced low stiffness of the sediment as well as low post peak shear strength. This requirement suggests that sediments hosting contraction-driven shear faults most likely have high porosity and high clay fraction and have undergone diagenetic reactions involving significant mineral dissolution. The diagenetic evolution of the sediment and its current composition may explain the global scaling relationship between the measured displacement and fault height for polygonal fault systems.

Citation: Shin, H., J. C. Santamarina, and J. A. Cartwright (2010), Displacement field in contraction-driven faults, *J. Geophys. Res.*, *115*, B07408, doi:10.1029/2009JB006572.

1. Introduction

[2] The structural analysis of tectonic normal fault systems is widely based on mechanical boundary conditions that faults experience in a regional or local tectonic context in which lateral confinement is locally reduced by lateral extension [e.g., *Ramsey and Lisle*, 2000]. However, not all normal faults can be considered with these classical boundary conditions.

[3] Polygonal faults are a notable exception: they are widely accepted to form during shallow burial, in tectonically passive settings, and under no lateral extension i.e., in strong contrast to the conditions for tectonic normal faulting [*Cartwright and Lonergan*, 1996; *Cartwright et al.*, 2003; *Nicol et al.*, 2003]. Polygonal faults also represent a major challenge for soil mechanics: they are an expression of shear failure, hence the stress path cannot follow the classical 1D k_0-stress condition that would prevail under zero-lateral strain conditions. Polygonal faults occur widely in passive continental margin basins where hydrate resources are contained [e.g., *Berndt et al.*, 2003], and occur pervasively in sediments that constitute the major sealing sequences for petroleum accumulations [e.g., *Watterson et al.*, 2000; *Stuevold et al.*, 2003; *Cartwright et al.*, 2007]. Therefore, the understanding of polygonal fault systems can be of crucial importance.

[4] In this paper we explore the displacement field on normal faults where the system is laterally confined i.e., the widely agreed boundary condition for polygonal faults. We start by reviewing the genesis of polygonal faults, followed by description of displacement data collected from a wide range of polygonal fault systems. Then, we present analytical results and numerical simulations of a single contraction-driven normal fault embedded in uncemented sediments. We build our understanding on previous numerical studies that showed agreement between natural displacement fields and those obtained in models where the elastic strain accumulation results from remote loading of a medium with an embedded shear plane [*Eshelby*, 1957; *Pollard and Segall*, 1987; *Burgmann et al.*, 1994; *Willemse et al.*, 1996]. As part of the study, we evaluate the material properties that are required to justify the magnitude of displacements typically observed in polygonal fault systems worldwide.

2. Genesis of Contraction-Driven Faults

[5] The precise mechanism leading to the formation of polygonal faults has been widely debated. Current models include gravitational instability and overturn due to rapid loading [*Henriet et al.*, 1991; *Watterson et al.*, 2000], contraction due to syneresis [*Cartwright and Dewhurst*, 1998], gravity sliding [*Higgs and McClay*, 1993], and mineral dissolution during early diagenesis [*Shin et al.*, 2008].

[6] A theoretically plausible failure mechanism must satisfy the general observation that polygonal faults begin to form in the first tens of meters of burial [*Cartwright et al.*, 2003;

[1]Civil and Environmental Engineering, University of Ulsan, Ulsan, South Korea.
[2]Civil and Environmental Engineering, Georgia Institute of Technology, Atlanta, Georgia, USA.
[3]3D Lab, School of Earth, Ocean and Planetary Sciences, Cardiff University, Cardiff, UK.

0148-0227/10/2009JB006572

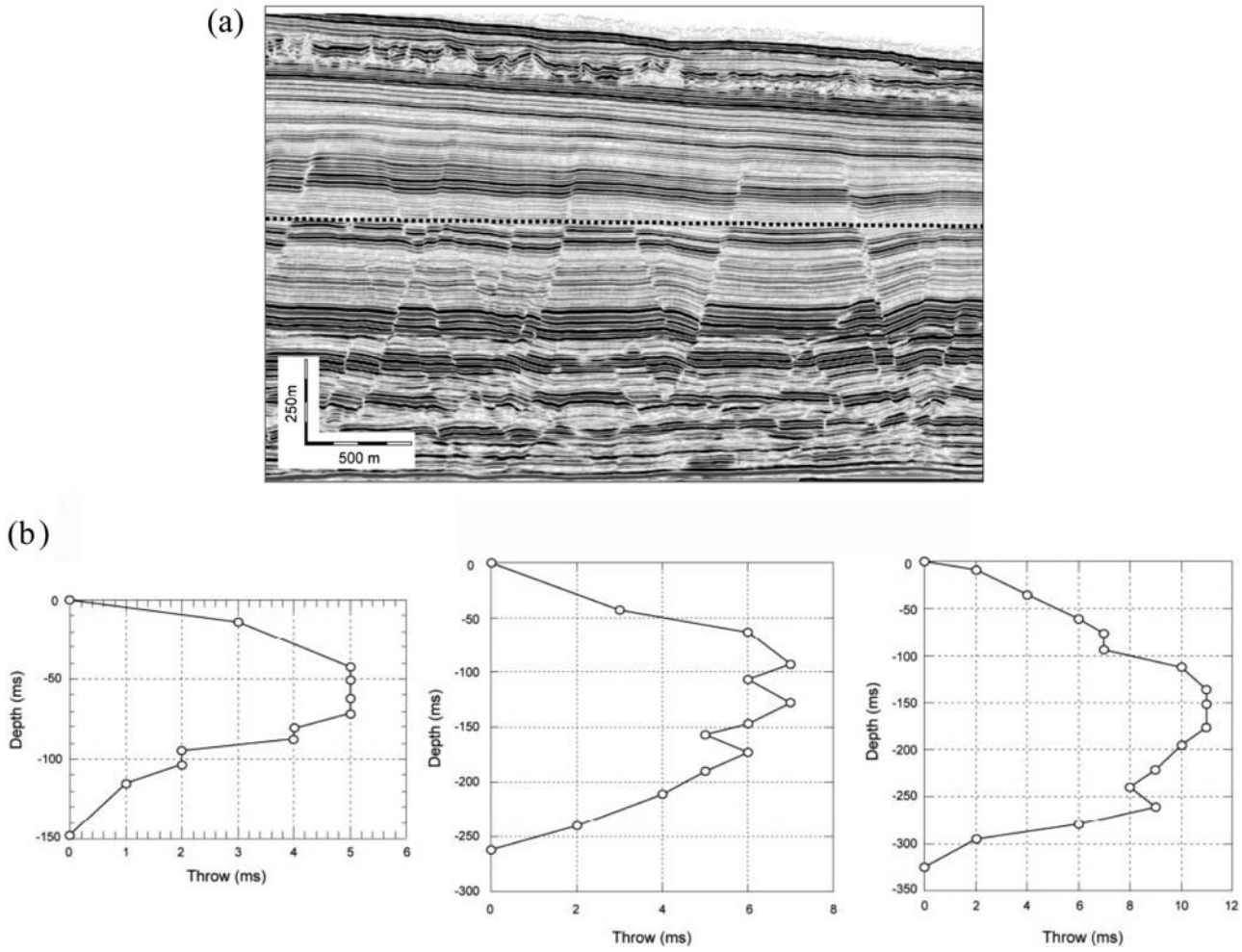

Figure 1. Polygonal fault system and its characteristic displacement versus depth profiles. (a) Seismic profile showing the typical geometry of polygonal faults in clay-rich sediments offshore Norway. The seabed is at the top of the image. The faults have maximum throw values close to the centers of the fault planes. Many of the faults exhibit small-scale folding close to the fault planes. The dotted line is a pre-faulting datum to allow the relative displacement across faults to be assessed. (b) Plots of throw (in milliseconds two-way travel time) versus depth (in milliseconds; note that 1 ms is approximately 1 m) for three faults from a polygonal fault system offshore west Africa. These plots all exhibit a central maximum and are hybrid between the end-member C and M types of *Muraoka and Kamata* [1983].

Gay et al., 2004]. The recent model proposed by *Shin et al.* [2008] demonstrates that mineral dissolution at zero lateral strain brings the state of the stress from the k_0-condition to the Coulomb active failure k_a-condition, thus triggering sediment failure. *Shin et al.* [2008] also show that shear displacement can localize under these stress conditions when the sediment exhibits post peak strain softening, and listed multiple soil conditions that exhibit this behavior. Low residual friction on polygonal fault planes is one possible mechanism to explain the displacement accumulation, as identified by *Goulty* [2002, 2008] and *Goulty and Swarbrick* [2005]. However, low residual friction does not explain the genesis of faults or the localization of shear into planes, and this model must also explain the magnitude of the observed displacement fields associated with polygonal faults for the range of physical properties that capture the diversity of sediment types in which polygonal faults are hosted. Furthermore, the deviatoric stress after fault slippage must be compatible with the failure criterion and boundary conditions. The analyses presented herein satisfy equilibrium and compatibility requirements.

3. Field Observations

[7] The displacement distributions in polygonal fault systems are obtained from 3D marine seismic surveys of shallow-buried sedimentary successions in different basins (an example is shown in Figure 1a). Data reduction typically involves depth conversion from two way travel time information using interval velocities derived from seismic data processing or from borehole petrophysics. It is assumed that the motion is dominantly dip-slip in these steep fault planes where the fault plane dip is typically $\beta > 60°$ [*Lonergan et al.*, 1998; *Cartwright et al.*, 2003; *Nelson*, 2007]. Minor oblique slip motion cannot be excluded, particularly close to high angle fault intersections in the lateral tip regions.

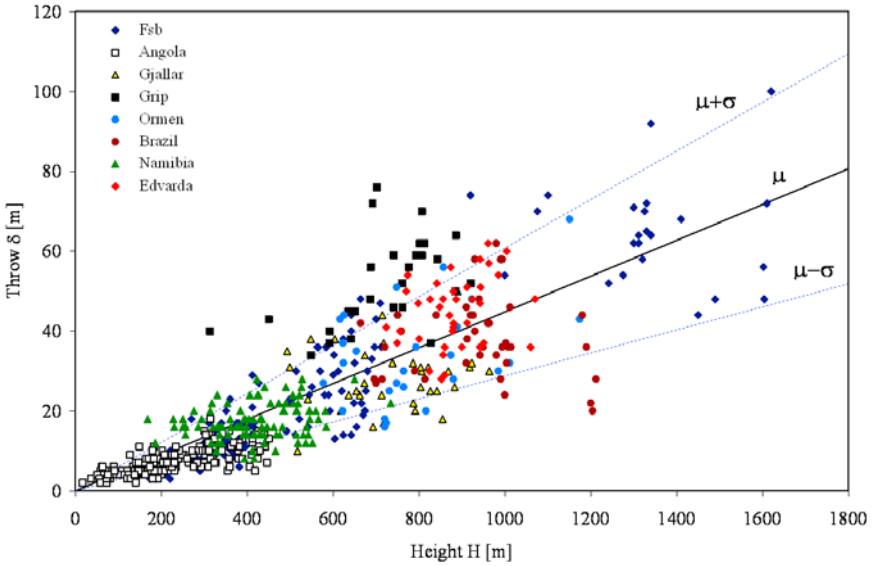

Figure 2. Height versus maximum throw for 629 faults from nine separate polygonal fault systems worldwide. Polygonal faults in these nine areas have not been deeply buried, and their upper tips are within 20–300 m of the surface. Most of the data are bounded within $\delta/H = 0.045 \pm 0.016$.

[8] Characteristic displacement-versus-depth profiles for polygonal faults are presented in Figure 1b in the form of throw δ versus depth z plots (herein, throw δ refers to the displacement along the fault plane projected onto the vertical direction). These examples are drawn from areas where the fault array is relatively open, i.e., where the majority of the lateral tips are not developed as hard-linked intersections [cf. *Nicol et al.*, 2003]. They typically show a maximum throw near the center of the fault, and the vertical displacement variation is similar in many respects to that observed for blind, tectonic normal faults in shallow-buried sedimentary sequences (see *Baudon and Cartwright* [2008b] for a detailed review). However, unlike tectonic normal faults, they are typically strata-bound, and are organized into 'tiers', with the vast majority of upper and lower tips occurring at a particular stratigraphic datum, or close to that datum [*Cartwright and Dewhurst*, 1998], suggesting a strong lithological control to their propagation [cf. *Nicol et al.*, 1996].

[9] The vertical displacement variation observed on many polygonal faults exhibits the classical end-member forms of C-type or M-type configurations where the displacement maximum has the form of a sharp peak or a broader set of plateau values [*Muraoka and Kamata*, 1983; *Walsh and Watterson*, 1988]. In typical blind normal faults and polygonal faults, the displacement patterns are commonly symmetric with depth. Notable exceptions are when a weak layer is present near the base or where a shallow propagating fault approaches the free surface (sediment-water interface); in these cases, a significant increase in local displacement gradients is generally observed [e.g., *Watterson et al.*, 2000; *Nicol et al.*, 2003; *Stuevold et al.*, 2003].

[10] Furthermore, the cross-sectional geometry of polygonal faults is remarkably similar to that of small tectonic normal faults. When observed close to their original position i.e., with their upper tips close to the modern seabed, they are generally planar (e.g., Figure 1a), and exhibit a range of fault plane dips from 50 to 80° [*Cartwright et al.*, 2003]. Once buried and inactive, they are passively flattened by vertical compaction, and have much shallower dips, often in the range of 30–50° [*Lonergan et al.*, 1998; *Stuevold et al.*, 2003]. In planform, they can be linear or highly curved, reflecting variations in lithology or mechanical interactions between neighboring faults during propagation [*Lonergan et al.*, 1998; *Goulty*, 2008].

[11] The regions surrounding individual polygonal faults show evidence of local strain accumulation that closely matches the theoretically predicted near-field strain for blind normal faults [*Barnett et al.*, 1987]. A good example of this strain distribution is seen in Figure 1a, where stratal reflections in the hanging wall are deflected below the regional datum. The zone of near-field strain varies from fault to fault, but its lateral extent away from the fault in both hanging wall and footwall locations is usually between 10 and 50% of the fault height. The strain is manifested in stratal rotation and deflections below and above regional, and also in localized thinning, particularly in the lower hanging wall quadrant of the fault [cf. *Barnett et al.*, 1987, Figure 1c]. The magnitude of these near field strains reaches a maximum close to the fault plane where it effectively equals the strains measured parallel to the fault in the presumed slip direction (the dip-slip condition of *Walsh and Watterson* [1988] and *Ramsey and Lisle* [2000]). There may be local oblique slip close to intersections, and material movements may take place out of the plane of maximum dip direction. However, the pattern of strain in the central portions of individual faults varies only gradually along strike, and is suggestive of dominantly dip-slip kinematics.

[12] Tectonic normal faults are widely considered to follow a simple scaling relationship between maximum displacement and maximum dimension [*Cowie and Scholz*, 1992; *Schultz et al.*, 2006]. For comparison, we plot the maximum throw δ versus fault height H in Figure 2 for a collection of

629 faults in polygonal systems worldwide (Note: height H is measured in the vertical direction). These data were selected from polygonal fault arrays where the vertical displacement variation was generally symmetric about a mid-point (see Figure 1b), and where there was little evidence of anomalously weak layers near the base because they distort displacement distribution on individual faults [*Watterson et al.*, 2000]. Similarly, the aspect ratio of faults is known to impact scaling relationships for faults [*Nicol et al.*, 1996], hence, these data come from faults with aspect ratios strike length-to-height between 0.8 and 2.6. It is likely that the data scatter may be partly due to interactions between faults which have the potential to retard tip-line propagation in some cases [*Nicol et al.*, 2003]; to minimize this effect, we selected faults where either or both their lateral tips were not involved in hard-linked intersections. Most of the data in Figure 2 are bound within δ/H = 0.045±0.016. These are surprisingly large displacements for systems that have not experienced extension in their basal planes; furthermore, δ/H values are larger than for most tectonic normal faults (as compared to trends in the work by *Cowie and Scholz* [1992] at an effective stress $\sigma' < 40$ MPa), even allowing for the use of H instead of the more typical strike length measurement of many scaling studies. We note that polygonal faults from areas with anomalously weak basal layers, or where there is a high degree of lateral intersection commonly have values of δ/H~0.1-to-0.2 which are significantly larger than those shown in Figure 2. The following sections attempt to model the displacement distribution observed in polygonal fault systems.

4. Analyses

[13] Our analysis of strain accumulation adopts a simple geometrical configuration reminiscent of the earlier studies, but we select material parameters and boundary conditions that apply to granular materials such as soils or uncemented sediments. Most importantly, our remote driving stress is gravitational loading under zero-lateral strain conditions, in order to replicate those suggested in recent models for polygonal fault growth [*Goulty*, 2008]. The approach is two dimensional and it does not capture the full complexity of lateral propagation effects of a three-dimensional array of normal faults that typifies polygonal fault systems; to minimize this limitation, we compare our model results with displacement values measured specifically from polygonal faults that exhibit the minimum observable evidence of lateral interaction, and no obvious distorting effects of anomalously weak layers within the deforming interval. Furthermore, our modeling does not capture the full complexity of propagation effects such as upper and lower tips in boundary layers or complex rheological stratification. Nevertheless, we consider that these limitations do not invalidate our primary conclusions regarding first-order estimates of the material properties necessary to justify the observed field strain in polygonal fault systems.

[14] Studies of the dip of normal faults in natural systems and shear localization in sediments suggest that the fault orientation β is dictated by the peak friction angle ϕ [*Walsh and Watterson*, 1988] (see review by *Vermeer* [1990]). Therefore, our analyses and simulations start by presuming a shear plane at $\beta = 45° + \phi/2$.

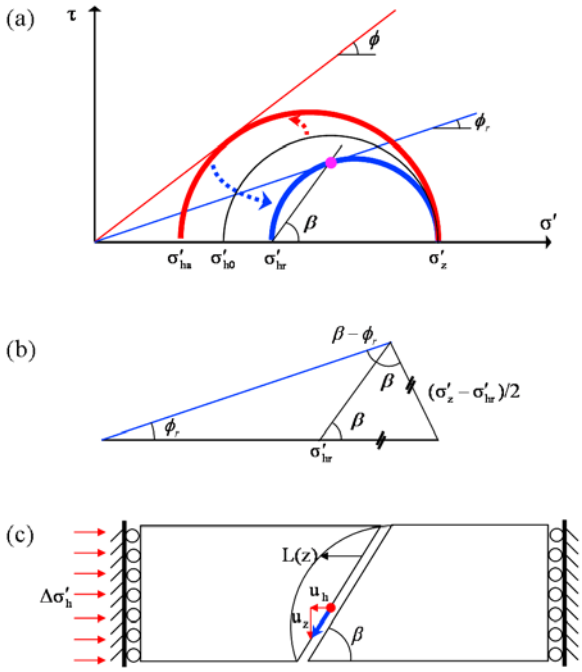

Figure 3. Equilibrium and compatibility analyses. (a) Stress path in the Mohr-Coulomb space. (b) Equilibrium at residual stress state. (c) Effective zone L(z) for horizontal strain accumulation and relative displacement compatibility along the fault slope.

[15] The stress redistribution caused by a residual friction angle $\phi_r < \phi$ acting on a fault at orientation $\beta = 45° + \phi/2$ leads to a new horizontal effective stress σ'_{hr} that is higher than the initial horizontal stress $\sigma'_{ho} = k_o\sigma'_z$. We can relate σ'_{hr} to the vertical effective stress so that $\sigma'_{hr} = k_r\sigma'_z$. Equilibrium dictates (Figures 3a and 3b)

$$k_r = \frac{\cos(\beta)\sin(\beta - \phi_r)}{\sin(\phi_r) + \cos(\beta)\sin(\beta - \phi_r)} \quad (1)$$

The horizontal stress change from the initial k_o-state to the final residual stress state $\Delta\sigma'_h = (k_r - k_o)\sigma'_z$ produces a contractive strain ε_h in the horizontal direction normal to the strike of the fault that can be estimated as

$$\varepsilon_h = \frac{\Delta\sigma'_h}{E} = (k_r - k_0)\frac{\sigma'_z}{E} \quad (2)$$

The effective horizontal length L(z) for strain accumulation away from the fault plane relates horizontal strain to horizontal displacement $u_h(z)$ as $u_h = \varepsilon_h/L$. We assume a parabolic function with depth $L(z) = z(1 - z/H)$, so that there is zero displacement at ends and the maximum length of influence is L(z) = H/4 on each side of the fault at a depth z = H/2, i.e., the effective zone for horizontal displacement around the fault is about half of fault height H (Figure 3c and *Barnett et al.* [1987]).

[16] An associated vertical displacement $u_z = u_h\tan\beta$ must take place to satisfy compatibility. The parabolic displacement field (in agreement with field trends in Figure 1b) is evaluated with the displacement constraints at the top and bottom of the fault, $u_z(z) = \varepsilon_h \tan\beta\, z(1 - z/H)$. The maxi-

mum throw δ along the fault is twice the relative displacement at the mid-height of the fault, $\delta = 2u_z(H/2)$; then

$$u_z(H/2) = \frac{H}{4}\varepsilon_h \tan(\beta) = \frac{(k_r - k_0)\tan(\beta)}{4}\frac{\sigma'_z}{E}H \quad (3)$$

Finally, the normalized throw δ/H becomes

$$\frac{\delta}{H} = \frac{(k_r - k_0)\tan(\beta)}{2}\frac{\sigma'_z}{E} \quad (4)$$

This order-of-magnitude expression predicts that the normalized throw δ/H increases linearly with the stress-to-stiffness ratio σ'_z/E and the normalized stress change k_r-k_o. The predicted displacement distribution along the fault has a parabolic shape with the maximum value at the mid-height. The maximum throw δ will be used to compare numerical results to field data.

[17] In the case of a surface fault, the normalized throw can be estimated using a fictitious height 2H, where H is the real height of the surface fault.

[18] Since the horizontal contractional strain at the base of the hanging wall is constrained by the surrounding medium, the volumetric strain around the tip of the fault is dominated by the vertical strain:

$$\varepsilon_v \approx \varepsilon_z = \left.\frac{\partial u(z)}{\partial z}\right|_{z=0} = \varepsilon_h \tan(\beta) \quad (5)$$

5. Numerical Study

[19] Numerical simulations are conducted to verify the previous analytical estimates (Section 4) and to gain additional insight into fault displacements and strain fields. In these simulations, we represent the sediment using the Drucker-Prager model where the Coulomb-type strength criterion is linearly proportional to the effective confining stress, i.e., we explicitly avoid cohesive strength so that effective stress dependent material parameters can be adopted particularly in the case of shallow faults. Constitutive model parameters and numerical simulation details including boundary conditions are summarized in Figure 4. A denser mesh is used near the fault (mesh size/fault height = 2/1000), which is simulated as a pre-existing single line of shear displacement fault elements with an orientation $\beta = 45° + \phi/2$ [*Goodman et al.*, 1968]. The initial friction angle ϕ in the fault elements is the same as in the surrounding elements. Fault formation starts from equilibrium conditions and consists of decreasing the friction angle of fault elements until the residual friction angle ϕ_r is reached (the friction angle is decreased at a rate of 0.05° per cycle to avoid numerical instabilities in this softening problem). The overburden load (q) for "deep faults" is applied on top of the sediment, under zero lateral deformation boundary conditions, and no additional body force is included because of the relatively small magnitude of stress relaxation compared to the overburden pressure; body force is imposed in shallow fault simulations, both for blind and surface faults (Figure 4).

[20] Two stiffness models are considered in this study to replicate likely end-member propagation modes for polygonal faults. The first model assumes that the fault height is much shorter than the burial depth, i.e., a deep blind fault, and the stiffness is considered constant in the region under study. This is intended to simulate the possible situation where polygonal faults first propagate as blind faults so that their tiplines do not intersect with another fault or feel the effects of a free surface. The second model applies to near-surface faults and the stiffness at depth z is assumed to be linearly dependent on the mean stress at that depth (linearity with effective stress applies to large strain processes such as those modeled here [*Terzaghi and Peck*, 1967]). This second case is intended to simulate the case where polygonal faults initiate within a few tens of meters of burial, and propagate to the free surface, where they subsequently behave as small syn-sedimentary faults, displacing the sediment-water interface (see examples in the work by *Stuevold et al.* [2003]). Results for both end-members are presented below together with a modification to incorporate addition of new load due to continued sedimentation during fault propagation.

5.1. Case 1: Constant Stiffness (Deep, Blind Faults)

[21] Predicted volumetric strains and throw are shown in Figure 5. The volumetric strain ε_v is normalized by the vertical load q at the burial depth and the constant sediment stiffness E. Likewise, throw δ is normalized by fault height H. Results show a crude bilateral symmetry with upper footwall and lower hanging wall quadrants being regions of contractile straining, and upper hanging wall and lower footwall regions experiencing unloading and expansion. This trend equates to deflections of originally horizontal stratal surfaces from their regional datum (Figure 1b). The volumetric strain field shown in Figure 5a bears a striking resemblance to strain fields published in previous studies [*Barnett et al.*, 1987; *Pollard and Segall*, 1987].

[22] The normalized throw $(\delta/H)(E/q)$ overlaps for all cases simulated with different E/q values in this study (E/q = 0.1, 1, 10, 100). In other words, the maximum throw δ in a given fault is directly proportional to the fault height H, the overburden stress q and inversely proportional to the sediment stiffness E (Figure 5). This observation confirms the possibility of crude scaling between δ and H for polygonal faults as discussed above (equation (3)). Once again, we find that although all models show strain distributions that match those associated with natural polygonal faults, small stiffness is required to match the observed natural strain magnitudes.

[23] The effect of peak friction angle, fault orientation and residual friction angle on throw and maximum volumetric strains around the fault are explored in Figures 5b and 6. It can be observed that the steeper faults with higher peak friction angle lead to higher normalized throws at the same residual friction angle (Figure 6a). The magnitude of the throws with the peak friction is well matched with the theoretical solution (equation (3)), except for the sediments with very high peak friction angle ($\phi \geq 50°$) where the numerical solution captures geometric constraints not considered in the analytical solution: eventually, a fault at right angle $\beta = 90°$ would have no slippage or horizontal stress change. The maximum volumetric strain values of the four quadrant regions are reasonably well matched by the analytical approximation (equation (4)), except at very high peak friction angle (Figure 6b).

[24] The maximum throw and the volumetric strain are directly related by the residual friction angle, because it determines the stress change the medium will experience after

Geometry and boundary conditions

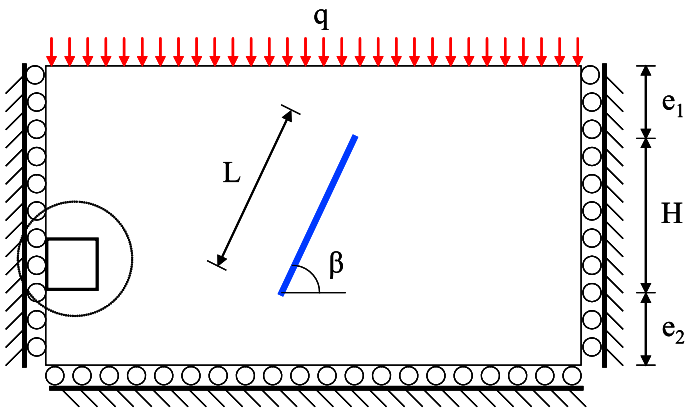

Element type

- Element type: 8 nodes, 2D plane strain
- Number of elements: 10,300
- No friction against boundaries
- Overburden stress on the top boundary

  (1) Deep faults: overburden = q (Fig. 4, 5 & 7a)

  (2) Shallow faults: overburden = zero (Fig. 6 & 7b-c-d)

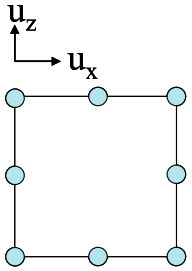

Material properties

- Constitutive model: Drucker-Prager model with non-associated flow rule
- Soil strength: Coulomb $\tau=\sigma' \tan \phi$, peak and residual friction angles ϕ and ϕ_r, zero cohesion.
- Stiffness models

  (1) Deep faults: E=constant, Poisson's ratio $\nu=0.3$ (Fig. 4, 5 & 7a).

  (2) Shallow faults: E/σ'_m=constant where $\sigma'_m=(\sigma'_1+\sigma'_2+\sigma'_3)/3$ and $\nu=0.3$ (Fig. 6 & 7b-c-d).

- Initial state of stress $k_0= \sigma'_x/\sigma'_z =1-\sin \phi$.
- Fracture orientation $\beta=45°+\phi/2$.

Figure 4. Numerical study: boundary conditions, model, and material parameters.

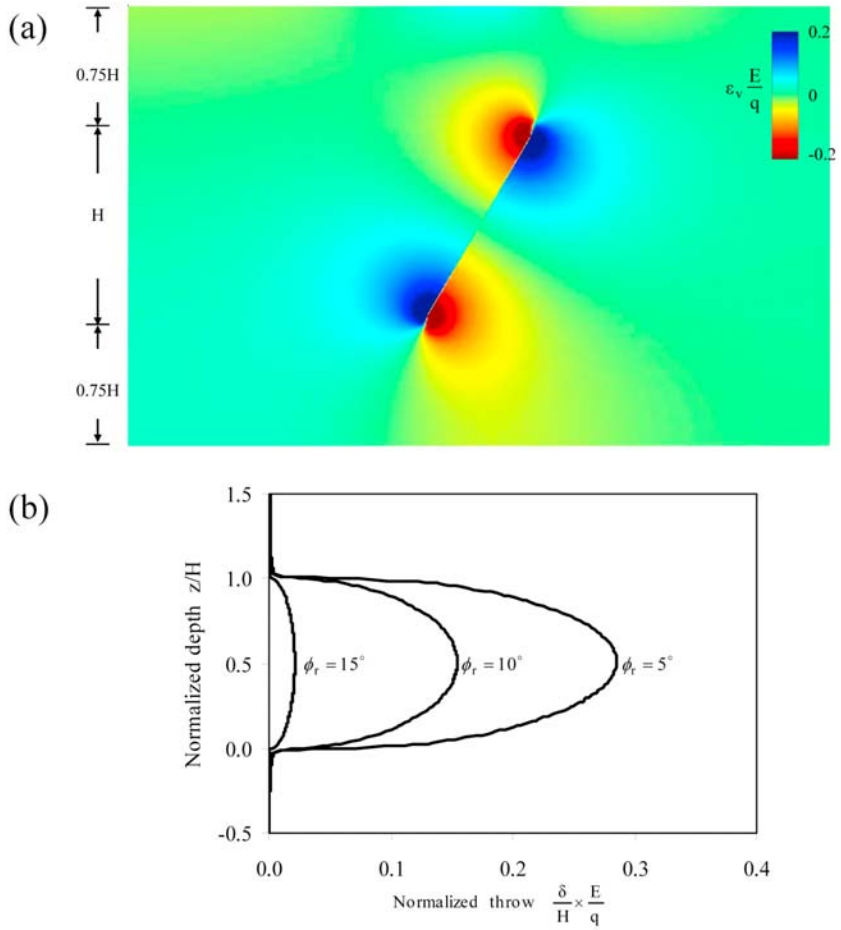

Figure 5. Strain and displacement field after fault slippage for a medium with constant stiffness E = constant (resembles deep burial condition). (a) Normalized volumetric strain $\varepsilon_v E/q$ (contractive is positive, blue). (b) Normalized throw along the fault length for different residual friction angles. Model parameters: sediment friction angles $\phi = 30°$, $\phi_r = 5°$, initial state of stress $k_0 = 1 - \sin\phi = 0.5$, fracture orientation $\beta = 45° + \phi/2 = 60°$. Distance to boundaries $e_1 = e_2 = 0.75H$ (refer to Figure 4 for model details).

fault propagation (equation (3)). The decrease in friction angle from the peak ϕ to the residual ϕ_r is strongly related with mineralogy: ϕ_r in kaonite > illinte > montmorrilonite. Furthermore, the volume fraction of platy clay particles must exceed 10~15% for a significant strain softening behavior to develop [*Kenney*, 1959; *Olson*, 1974; *Lupini et al.*, 1981; *Skempton*, 1985; *Mesri and Cepeda-Diaz*, 1986]. The effect of the residual friction on the displacement field, the magnitude of the normalized throw, and the volumetric strain is reported in Figures 5b, 6a and 6c. It can be observed that both the normalized throw and the volumetric strain increase as the residual friction decreases. The volumetric strain of the four quadrant regions retains the near bilateral symmetry (Figure 6b).

5.2. Case 2: Proximity to a Free Surface

[25] These simulations are conducted with the second stiffness model E/σ'_m = constant to approximate the inherent stress-dependent sediment stiffness at large strains. Proximity to the free surface markedly affects the strain pattern, particularly as the normalized burial depth $e_1/H < 0.5$ (sketch in Figure 4). When the fault intersects the surface, contractional strains develop along the entire hanging wall, and only dilatant strains take place in the lower footwall. Fur-

Figure 6. Effect of peak and residual friction on the strain and displacement field in a sediment of constant stiffness, E = constant (deep fault). (a) Maximum throw for different peak and residual friction angles. Theoretical trends (solid lines) are computed for different values of the friction angle ϕ and residual friction angle ϕ_r using equation equation (4) where k_r is computed with equation (1). (b) Maximum volumetric strains near the fault ends for different peak friction angles (see insert). Theoretical lines show predictions made using equation (5) where the horizontal strain is computed with equation (2). (c) Volumetric strains near the fault ends as a function of residual friction angle. Model parameters: initial state of stress $k_0 = 1 - \sin\phi$, fracture orientation $\beta = 45° + \phi/2$. Distance to boundaries $e_1 = e_2 = 0.75H$; refer to Figure 4 for model details.

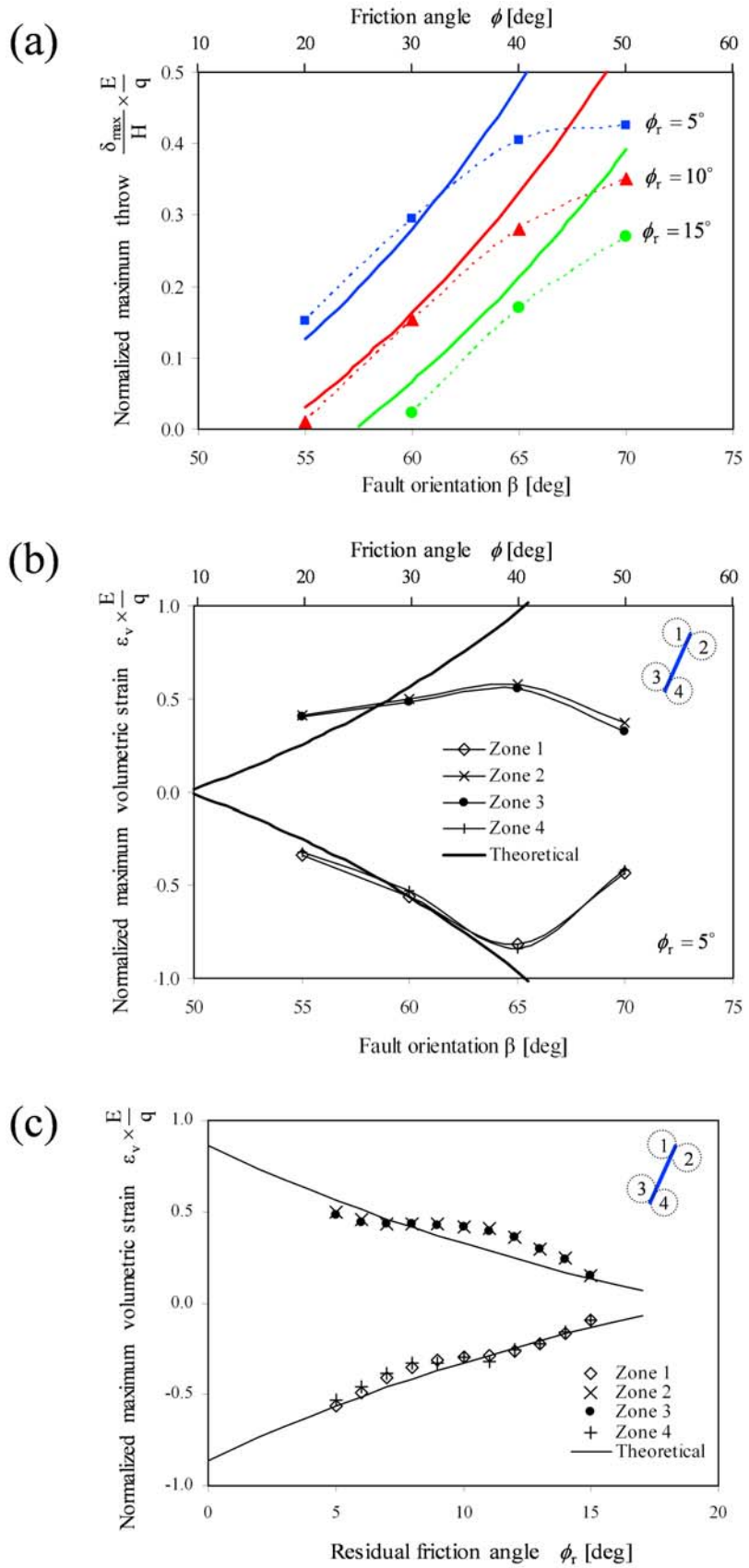
(a)
Friction angle ϕ [deg]
10 20 30 40 50 60
Normalized maximum throw $\frac{\delta_{max}}{H} \times \frac{E}{q}$
0.5 0.4 0.3 0.2 0.1 0.0
$\phi_r = 5°$
$\phi_r = 10°$
$\phi_r = 15°$
50 55 60 65 70 75
Fault orientation β [deg]
(b)
Friction angle ϕ [deg]
10 20 30 40 50 60
Normalized maximum volumetric strain $\varepsilon_v \times \frac{E}{q}$
1.0 0.5 0.0 0.5 1.0
1 2 3 4
Zone 1
Zone 2
Zone 3
Zone 4
Theoretical
$\phi_r = 5°$
50 55 60 65 70 75
Fault orientation β [deg]
(c)
Normalized maximum volumetric strain $\varepsilon_v \times \frac{E}{q}$
1.0 0.5 0.0 -0.5 -1.0
1 2 3 4
Zone 1
Zone 2
Zone 3
Zone 4
Theoretical
0 5 10 15 20
Residual friction angle ϕ_r [deg]

Figure 6

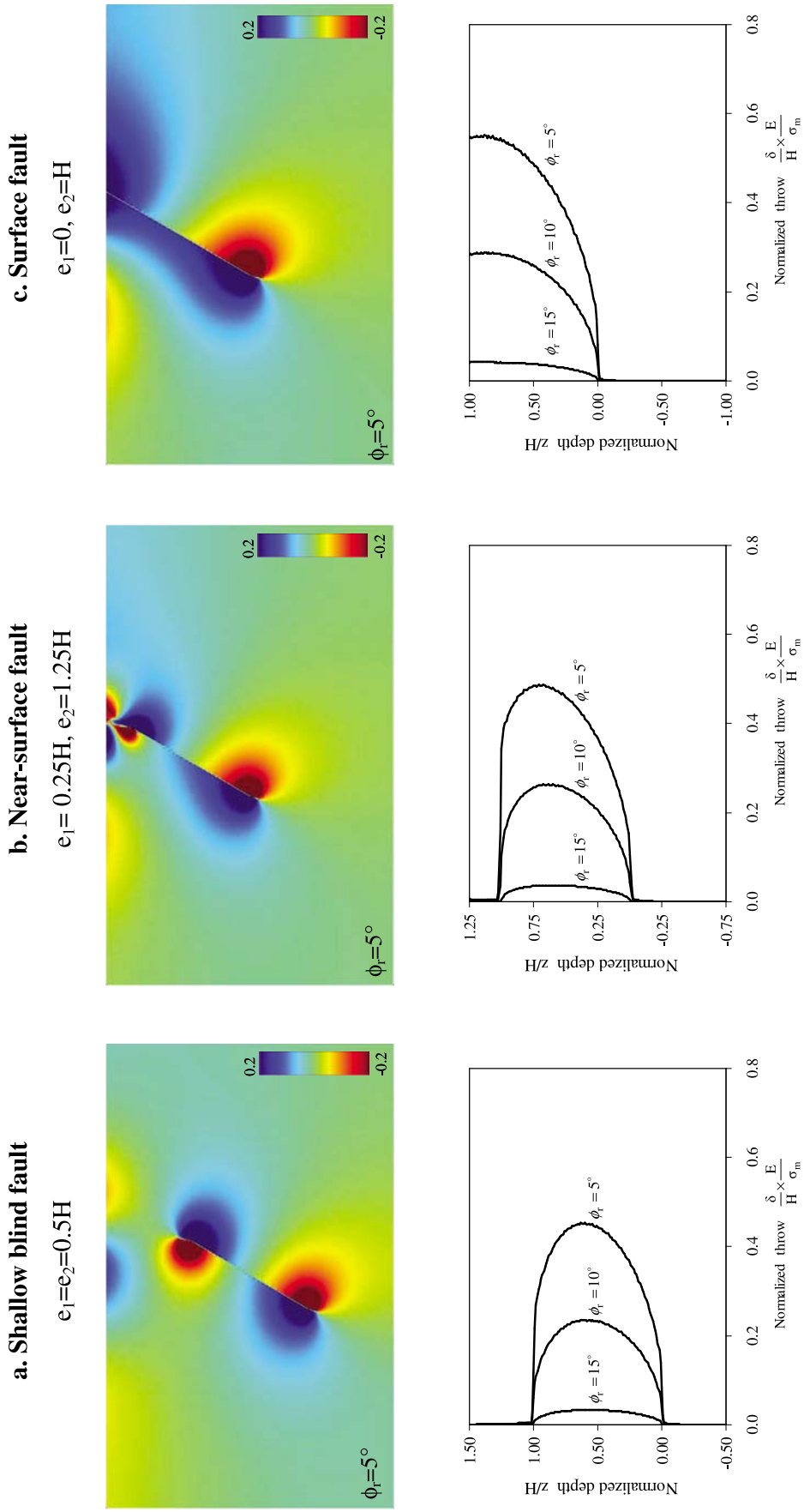

Figure 7. Proximity of a shallow fault to a free upper boundary. Effect on displacement along the fault and volumetric strain: (a) blind fault, (b) near-surface fault, and (c) surface fault. Other boundary conditions in Figure 4. The sediment stiffness increases with depth in the three cases E/σ_m = constant, in agreement with shallow fault conditions. Model parameters: sediment peak friction angle $\phi = 30°$, initial state of stress $k_0 = 1 - \sin\phi = 0.5$, fracture orientation $\beta = 45° + \phi/2 = 60°$. Distance to boundaries noted in each column; refer to sketch in Figure 4.

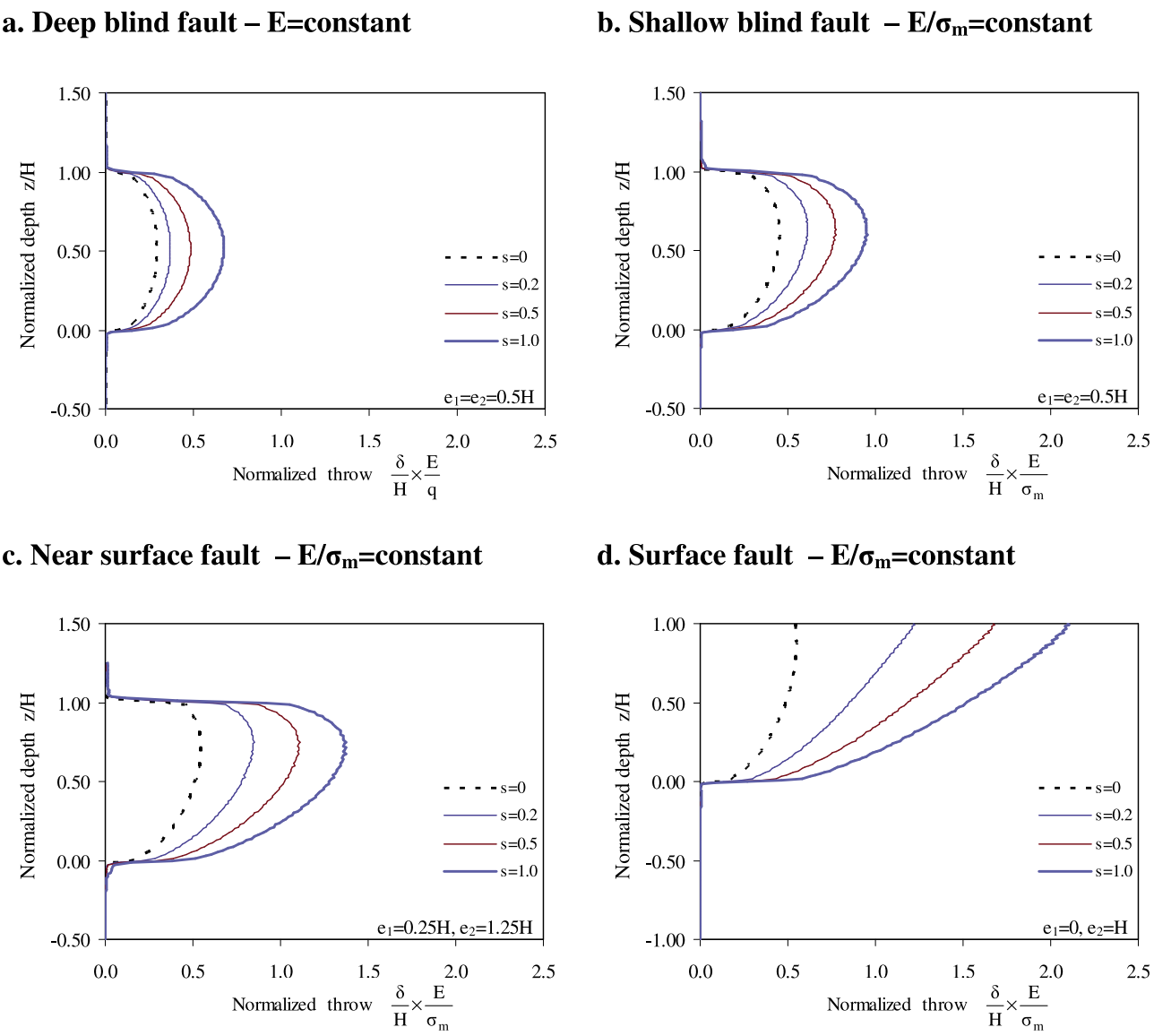

Figure 8. Effect of additional surface load on the development of displacements along the fault. The additional vertical stress is normalized by the initial vertical stress at the bottom of the model s = $\Delta\sigma'_z/\sigma'_{zo}$. Model parameters: sediment peak friction angle ϕ = 30°, residual friction angle ϕ_r = 5°, initial state of stress $k_0 = 1 - \sin\phi = 0.5$, fracture orientation $\beta = 45° + \phi/2 = 60°$. Distance to boundaries noted in each plot; refer to Figure 4 for model details.

thermore, interaction of the fault with the free surface significantly modifies the geometry of displacements in the near-field to the fault, leads to greater asymmetry in fault displacements, and causes an increase -albeit minor- in the maximum throw (Figure 7). This pattern of displacement variation is similar in many respects to that observed for small synsedimentary normal faults [e.g., *Childs et al.*, 2003; *Baudon and Cartwright*, 2008a], although exact comparison is difficult because the timing of the transition from blind propagation to free-surface intersection is unknown in the natural examples.

5.3. Case 3: Additional Loading After Fault Formation

[26] Additional sedimentation is simulated as a load-controlled boundary condition imposed on the sediment surface. Sedimentation after fault formation causes further displacement along the fault in both deep and shallow faults. The additional stress applied $\Delta\sigma'z$ is normalized by the initial vertical stress at the base of the modeled region σ'_{zo} in each case, s = $\Delta\sigma'_z/\sigma'_{zo}$, in other words, a value of s = 1 implies doubling the burial depth at the base. Results summarized in Figure 8 show the pronounced increase in fault displacement, particularly for the near surface faults. This indicates that additional gravitational loading onto pre-existing faults could be sufficient to maintain active slip conditions, provided that the requisite material properties apply for the granular medium and fault plane, respectively. The corollary of this is that cessation of additional sedimentation should cause the fault to become inactive, unless added complexity

such as further changes in material properties or secondary consolidation (creep) are considered explicitly.

6. Discussion

[27] This study has attempted to simulate natural strain accumulation in polygonal faults, albeit using a 2D approach, and to determine the relative relevance of controlling factors with respect to the strain distribution and magnitude. Even with the uncertainties implied by using a 2D simulation of three-dimensional fault systems, model results reveal important first-order behavior of simple normal faults under gravitational loading.

[28] Results obtained for the end-member cases of blind and surface faults, show that continued slip on a normal fault can occur entirely due to vertical loading, even though there is no net extension. This fundamentally differs from classical views of normal fault growth in which a driving stress is required to maintain conditions of fault activity, and where that drive involves a true tectonic extension. This alternative growth mechanism to normal faulting is therefore entirely compatible with the boundary kinematic conditions for polygonal fault growth in many natural settings, as first suggested by *Goulty* [2002]. However, the strain magnitude observed in natural polygonal fault systems is sufficiently large, that both the theoretical and modeling approaches undertaken here suggest that a very low value of stiffness is implied, along with a requirement for strain softening behavior. The question therefore arising, is under what conditions can these physical property requirements be met such that the typical strains can thus accumulate? The following analysis demonstrates that strain softening and low stiffness are most likely to be encountered as the natural response of sediments that have experienced mineral dissolution.

6.1. Strain Softening After Dissolution: Effective Stress Analysis

[29] Analytical and numerical studies presented earlier assumed a low residual friction angle. Further insight is gained by anticipating the evolution of dissolution and failure in the four main dimensions that capture sediment behavior (Figure 9): effective confinement σ' or mean stress $p' = (\sigma'_1 + \sigma'_3)/2$, shear stress τ or deviatoric stress $q = (\sigma'_1 - \sigma'_3)/2$, axial strain ε_a, and void ratio e. Note that p′-q define the apex of the Mohr circle, and that the axial strain is determined by volume change in one dimensional loading $\varepsilon_a = -\Delta e/(1 + e_0)$. Two types of sediment responses experiencing mineral dissolution are plotted in Figure 9. We first consider starting with the drained failure case (Figure 9a, interpretation based on work by *Shin et al.* [2008] and *Shin and Santamarina* [2009]):

[30] 1. In the sedimentation stage, the sediment follows the normally consolidated line NCL to reach point 1 where the void ratio is in equilibrium with the overburden stress, and the initial horizontal stress is $\sigma'_{h0} = k_0\sigma'_z$ where $k_0 \approx 1 - \sin\phi$ according to Jaky's equation [*Jaky*, 1944].

[31] 2. In the diagenesis stage, dissolution increases the void ratio to point 2 and lowers the horizontal stress to the failure condition $\sigma'_h \approx k_a\sigma'_z$ where $k_a = \tan^2(45° - \phi/2)$. Note that the soil mass is at the verge of failure in τ-σ', yet away from the critical state line CSL in the e-σ' space.

[32] 3. In the drained failure stage, the sediment shears and collapses, and often returns to a state similar to k_0 (path from 2 to 3). The void ratio may end near the NCL or even the CSL lines (point 3).

[33] We next consider a second case, and explore the undrained shear and collapse of the sediment following dissolution (Figure 9b). Points 1 and 2 are the same as in the previous case, then

[34] 4. In the undrained failure stage, the undrained shear and collapse occurs at constant volume, and the sediment evolves toward the critical state line at constant void ratio, as shown by point 3 in the e-σ' quadrant. There is a high increase in pore pressure due to the high porosity in partially dissolved sediments prior to failure. The effective stress σ' decreases and so does the strength according to the Coulomb criterion $\tau_{ult} = \sigma' \tan\phi$, therefore, there is pronounced strain softening.

[35] 5. In the pressure diffusion stage, after shear, the excess pore pressure dissipates with time, and the sediment evolves toward a reconsolidated stress probably near the normally consolidated line NCL (dotted lines beyond point 3).

[36] Note that post failure strain softening is observed in both cases (trajectories from points 2 to 3), and there is no need to involve low residual friction angle ϕ_r to justify shear localization. In any case, low ϕ_r will contribute to localization and strain accumulation.

[37] It is also important to recognize that the sediment at points 1 and 2 may be profoundly different. For example, fresh volcanic ash is made of silt and sand size amorphous silica and packs at void ratio e = 0.8 to 1.7, yet, diagenesis may change it into a clay sediment made of halloysite, allophane and imogolite packed at a high void ratio e = 2-to-7 [*Herrera et al.*, 2007].

6.2. Low Equivalent Stiffness

[38] The ratio of normalized throw δ/H to normalized stiffness E/σ' in equation (3) is a function of ϕ and ϕ_r. For a wide range of parameters ($30° \le \phi \le 40°$ and $5° \le \phi_r \le 15°$), the normalized stiffness must be between $1.5 < E/\sigma'_z < 10$ to match field data $\delta/H \approx 0.045$. This is a surprisingly low number in sediments where E/σ' values range from $E/\sigma' \sim 10^3$ for small strains to $E/\sigma' \sim 40$ at large strains [*Santamarina et al.*, 2001]. In general, permutations of the main controlling parameters such as orientation, burial depth, and residual shear strength cannot match the strain magnitude observed on natural polygonal faults if typical values of sediment stiffness are used.

[39] Indeed, our results strongly imply that gravitational loading cannot by itself account for the significant deformations observed in polygonal faults, even for very low residual friction angles. Moreover, these extraordinary normal faults often occur on layers with zero basal extension, therefore fault displacements cannot be the result of extension and we cannot appeal to regional extensional kinematics to solve the strain magnitude problem [*Cartwright and Lonergan*, 1996].

[40] To resolve this difficulty, we consider the processes of dissolution proposed as a triggering mechanism by *Shin et al.* [2008] and examine whether it can also account for the strain observed in natural systems. Dissolution produces a sediment of high porosity prior to shear, as anticipated in Figure 9 and observed in experimental results with sand

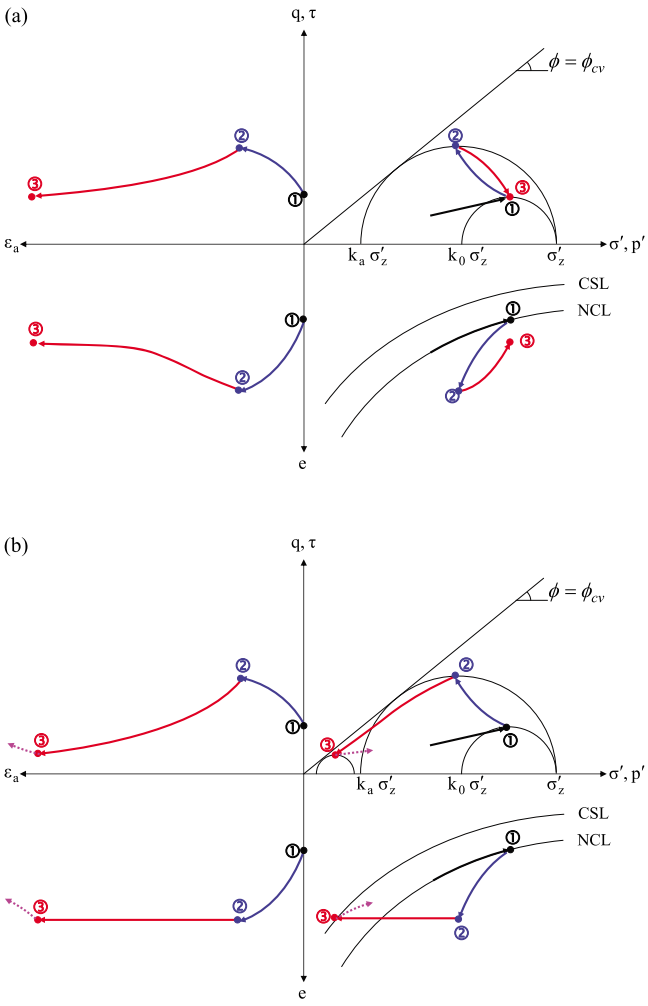

Figure 9. Evolution of stress and strain during mineral dissolution and fault formation: (a) drained failure and (b) undrained failure.

and salt mixtures and in discrete element simulations with mixtures of rigid and vanishing grains [*Shin et al.*, 2008; *Shin and Santamarina*, 2009]. Consider a sediment with void ratio e* after dissolution but prior to shear; if no global volumetric deformation takes place during dissolution, $e^* = (e_0 + \alpha)/(1 - \alpha)$ where e_0 is the initial void ratio prior to dissolution and α the dissolved volume fraction. If the void ratio after shear is consistent with either the NCL or CLS lines (Figure 9a), the normalized equivalent skeletal compressibility E_{eq}/σ' that governs volume contraction at fault formation can be estimated to a first approximation as

$$\frac{k_r - k_a}{\alpha} > \frac{E_{eq}}{\sigma'_z} > \frac{k_r - k_a}{\alpha + 0.3(1-\alpha)C_c/(1+e_0)} \qquad (6)$$

This expression predicts that the normalized stiffness is about $E_{eq}/\sigma' \approx$ 1.5-to-6 during shearing in sediments that have experienced α = 10% dissolution.

[41] The argument presented above has a further fundamental implication: it suggests that the strain accumulates in a material in which the stiffness is low to start, or is lowered incrementally as a function of time. This diagenetically "coupled" model for physical property evolution and stress development then offers an explanation for the fundamental and defining characteristic of polygonal fault systems, namely their polygonal planform geometry. To develop a truly polygonal system with the intersection relationships that are universally observed [*Nicol et al.*, 2003], it is clearly necessary that some faults nucleate and propagate earlier than others, and indeed the displacement transfer that occurs at intersections testifies to this simple principle [*Stuevold et al.*, 2003]. It follows from this that as one fault is reaching almost full propagation, and accumulating strain accordingly, others nearby are only just initiating. This temporal evolution of the network thus matches a driving mechanism that has an inbuilt time dependence, as would be inevitable with dissolution-based diagenesis.

7. Conclusions

[42] The genetic mechanism of polygonal fault systems has been extensively debated mainly due to the boundary constraints for fault mobilization, unlike tectonic normal faults.

[43] Mineral dissolution drives the in situ stress state from the initial at-rest k_0 condition to Coulomb-failure k_a condition, the sediment becomes inherently strain softening, conditions for strain localization are satisfied leading to fault formation, and the equivalent stiffness becomes sufficiently low to justify observed displacement fields. Indeed, displacements measured in polygonal fault systems can only be explained if the whole medium has stiffness much lower than the stiffness for standard sedimentary conditions.

[44] The throw δ in contraction-driven shear faults is proportional to the fault height H, and the initial effective stress in the sediment σ, and inversely proportional to the sediment stiffness E and the residual friction angle ϕ_r (or the post-peak strength).

[45] Proximity to a free upper boundary biases the displacement pattern (larger displacements near the boundary), but it does not have a pronounced impact on the magnitude of displacements during fault formation. Additional surface loading after formation causes further fault displacement; the effect is more pronounced when faults are closer to the free surface. Thus additional displacement may take place once a fault has formed by further decrease in ϕ_r (unlikely), further dissolution (i.e., decrease in E for the purpose of modeling), or additional surface loading.

[46] We anticipate that the ratio E/σ and the residual strength are directly related to the diagenetic evolution of the sediment and its current composition (mineralogy and fabric). Therefore, measured δ/H values in polygonal faults around the world may cluster once the sediment composition is taken into consideration.

[47] **Acknowledgments.** Support for this research was provided by National Science Foundation, Goizueta Foundation, Royal Society and Wolfson Foundation. Discussions with David James and Neil Goulty are greatly appreciated.

References

Barnett, J. A. M., J. Mortimer, J. H. Rippon, J. J. Walsh, and J. Watterson (1987), Displacement geometry in the volume containing a single normal fault, *AAPG Bull.*, *71*, 925–937.

Baudon, C., and J. Cartwright (2008a), Early stage evolution of growth faults: 3D seismic insights from the Levant Basin, eastern Mediterranean, *J. Struct. Geol.*, *30*, 888–898, doi:10.1016/j.jsg.2008.02.019.

Baudon, C., and J. A. Cartwright (2008b), 3D seismic characterisation of an array of blind normal faults in the Levant Basin, eastern Mediterranean, *J. Struct. Geol.*, *30*, 746–760, doi:10.1016/j.jsg.2007.12.008.

Berndt, C., S. Buenz, and J. Mienert (2003), Polygonal fault systems on the mid-Norwegian margin: A long-term source for fluid flow, in *Subsurface Sediment Mobilization*, edited by P. Van Rensbergen et al., *Geol. Soc. Spec. Publ.*, *216*, 283–290, doi:10.1144/GSL.SP.2003.216.01.18.

Burgmann, R., D. D. Pollard, and S. J. Martel (1994), Slip distributions on faults—Effects of stress gradients, inelastic deformation, heterogeneous host-rock stiffness, and fault interaction, *J. Struct. Geol.*, *16*, 1675–1690, doi:10.1016/0191-8141(94)90134-1.

Cartwright, J. A., and D. N. Dewhurst (1998), Layer-bound compaction faults in fine-grained sediments, *Geol. Soc. Am. Bull.*, *110*, 1242–1257, doi:10.1130/0016-7606(1998)110<1242:LBCFIF>2.3.CO;2.

Cartwright, J. A., and L. Lonergan (1996), Volumetric contraction during the compaction of mudrocks: A mechanism for the development of regional-scale polygonal fault systems, *Basin Res.*, *8*, 183, doi:10.1046/j.1365-2117.1996.01536.x.

Cartwright, J., D. James, and A. Bolton (2003), The genesis of polygonal fault systems: A review, in *Subsurface Sediment Mobilization*, edited by P. Van Rensbergen et al., *Geol. Soc. Spec. Publ.*, *216*, 223–243, doi:10.1144/GSL.SP.2003.216.01.15.

Cartwright, J. A., M. Huuse, and A. Aplin (2007), Seal bypass systems, *AAPG Bull.*, *91*, 1141–1166, doi:10.1306/04090705181.

Childs, C., A. Nicol, J. J. Walsh, and J. Watterson (2003), The growth and propagation of synsedimentary faults, *J. Struct. Geol.*, *25*, 633–648, doi:10.1016/S0191-8141(02)00054-8.

Cowie, P. A., and C. H. Scholz (1992), Physical explanation for the displacement length relationship of faults using post-yield fracture-mechanics model, *J. Struct. Geol.*, *14*, 1133–1148, doi:10.1016/0191-8141(92)90065-5.

Eshelby, J. D. (1957), The determination of the elastic field of an ellipsoidal inclusion, and related problems, *Proc. R. Soc. London, Ser. A*, *241*, 376–396, doi:10.1098/rspa.1957.0133.

Gay, A., M. Lopez, P. Cochonat, and G. Sermondadaz (2004), Polygonal faults-furrows system related to early stages of compaction: Upper Miocene to recent sediments of the Lower Congo Basin, *Basin Res.*, *16*, 101–116, doi:10.1111/j.1365-2117.2003.00224.x.

Goodman, R. E., R. L. Taylor, and T. L. Brekke (1968), Model for mechanics of jointed rock, *J. Soil Mech. Found. Div. Am. Soc. Civ. Eng.*, *94*, 637–659.

Goulty, N. R. (2002), Mechanics of layer-bound polygonal faulting in fine-grained sediments, *J. Geol. Soc.*, *159*, 239–246, doi:10.1144/0016-764901-111.

Goulty, N. R. (2008), Geomechanics of polygonal fault systems: A review, *Petrol. Geosci.*, *14*, 389–397, doi:10.1144/1354-079308-781.

Goulty, N. R., and R. E. Swarbrick (2005), Development of polygonal fault systems: A test of hypotheses, *J. Geol. Soc.*, *162*, 587–590, doi:10.1144/0016-764905-004.

Henriet, J. P., M. De Batist, and M. Verschuren (1991), Early fracturing of Palaeogene clays, southernmost North Sea: Relevance to mechanisms of primary hydrocarbon migration, in *Generation, Accumulation, and Production of Europe's Hydrocarbons*, *Eur. Assoc. Pet. Geosci. Spec. Publ.*, vol. 1, edited by A. M. Spencer, pp. 217–227, Oxford Univ. Press, Oxford, U. K.

Herrera, M. C., A. Lizcano, and J. C. Santamarina (2007), Colombian volcanic ash soils, in *Characterisation and Engineering Properties of Natural Soils: Proceedings of the Second International Workshop on Characterisation and Engineering Properties of Natural Soils, Singapore, 29 November–1 December 2006*, edited by T. S. Tan et al., pp. 2385–2409, Taylor and Francis, New York.

Higgs, W. G., and K. R. McClay (1993), Analogue sandbox modelling of Miocene extensional faulting in the Outer Moray Firth, in *Tectonics and Seismic Sequence Stratigraphy*, edited by G. Williams and A. Dobb, *Geol. Soc. Spec. Publ.*, *71*, 141–162, doi:10.1144/GSL.SP.1993.071.01.07.

Jaky, J. (1944), The coefficient of earth pressure at rest, *J. Union Hung. Eng. Archit.*, *78*, 355–358.

Kenney, T. C. (1959), Discussion of "Geotechnical properties of glacial lake clays," by T. H. Wu, *J. Soil Mech. Found. Div. Am. Soc. Civ. Eng.*, *85*, 67–79.

Lonergan, L., J. Cartwright, and R. Jolly (1998), The geometry of polygonal fault systems in Tertiary mudrocks of the North Sea, *J. Struct. Geol.*, *20*, 529–548, doi:10.1016/S0191-8141(97)00113-2.

Lupini, J. F., A. E. Skinner, and P. R. Vaughan (1981), The drained residual strength of cohesive soils, *Geotechnique*, *31*, 181–213, doi:10.1680/geot.1981.31.2.181.

Mesri, G., and A. F. Cepeda-Diaz (1986), Residual shear-strength of clays and shales, Geotechnique, 36, 269–274, doi:10.1680/geot.1986.36.2.269.

Muraoka, H., and H. Kamata (1983), Displacement distribution along minor fault traces, *J. Struct. Geol.*, *5*, 483–495, doi:10.1016/0191-8141(83)90054-8.

Nelson, M. (2007), 3D geometry and kinematics of non-colinear fault intersections, thesis, Cardiff Univ., Cardiff, U. K.

Nicol, A., J. Watterson, J. J. Walsh, and C. Childs (1996), The shapes, major axis orientations and displacement patterns of fault surfaces, *J. Struct. Geol.*, *18*, 235–248, doi:10.1016/S0191-8141(96)80047-2.

Nicol, A., J. J. Walsh, J. Watterson, P. A. R. Nell, and P. Bretan (2003), The geometry, growth and linkage of faults within a polygonal fault system from South Australia, in *Subsurface Sediment Mobilization*, edited by P. Van Rensbergen et al., *Geol. Soc. Spec. Publ.*, *216*, 245–261, doi:10.1144/GSL.SP.2003.216.01.16.

Olson, R. E. (1974), Shearing strength of kaolinite, illite, and montmorillonite, *J. Soil Mech. Found. Div. Am. Soc. Civ. Eng.*, *100*, 1215–1229.

Pollard, D. D., and P. Segall (1987), Theoretical displacements and stresses near fractures in rock: With applications to faults, joints, veins, dikes, and solution surfaces, in *Fracture Mechanics of Rocks*, edited by B. K. Atkinson, pp. 277–349, Academic, London.

Ramsey, J. G., and R. J. Lisle (2000), *The Techniques of Modern Structural Geology,* vol. 3, *Applications of Continuum Mechanics in Structural Geology*, Academic, London.

Santamarina, J. C., K. A. Klein, and M. A. Fam (2001), *Soils and Waves: Particulate Materials Behavior, Characterization and Process Monitoring*, 488 pp., John Wiley, Chichester, U. K.

Schultz, R. A., C. H. Okubo, and S. J. Wilkins (2006), Displacement-length scaling relations for faults on the terrestrial planets, *J. Struct. Geol.*, *28*, 2182–2193, doi:10.1016/j.jsg.2006.03.034.

Shin, H., and J. C. Santamarina (2009), Mineral dissolution and the evolution of k_0, *J. Geotech. Geoenviron. Eng.*, *135*, 1141–1147, doi:10.1061/(ASCE)GT.1943-5606.0000053.

Shin, H., J. C. Santamarina, and J. A. Cartwright (2008), Contraction-driven shear failure in compacting uncemented sediments, *Geology*, *36*, 931–934, doi:10.1130/G24951A.1.

Skempton, A. W. (1985), Residual strength of clays in landslides, folded strata and the laboratory, *Geotechnique*, *35*, 3–18, doi:10.1680/geot.1985.35.1.3.

Stuevold, L. M., R. B. Faerseth, L. Arnesen, J. Cartwright, and N. Moller (2003), Polygonal faults in the Ormen Lange Field, More Basin, offshore mid Norway, in *Subsurface Sediment Mobilization*, edited by P. Van Rensbergen et al., *Geol. Soc. Spec. Publ.*, *216*, 263–281, doi:10.1144/GSL.SP.2003.216.01.17.

Terzaghi, K., and R. B. Peck (1967), *Soil Mechanics in Engineering Practice*, 2nd ed., 729 pp., John Wiley, New York.

Vermeer, P. A. (1990), The orientation of shear bands in biaxial tests, *Geotechnique*, *40*, 223–236, doi:10.1680/geot.1990.40.2.223.

Walsh, J. J., and J. Watterson (1988), Analysis of the relationship between displacements and dimensions of faults, *J. Struct. Geol.*, *10*, 239–247, doi:10.1016/0191-8141(88)90057-0.

Watterson, J., J. Walsh, A. Nicol, P. A. R. Nell, and P. G. Bretan (2000), Geometry and origin of a polygonal fault system, *J. Geol. Soc.*, *157*, 151–162.

Willemse, E. J. M., D. D. Pollard, and A. Aydin (1996), Three-dimensional analyses of slip distributions on normal fault arrays with consequences for fault scaling, *J. Struct. Geol.*, *18*, 295–309, doi:10.1016/S0191-8141(96)80051-4.

J. A. Cartwright, 3D Lab, School of Earth, Ocean and Planetary Sciences, Cardiff University, Main Building, Park Place, Cardiff CF10 3YE, UK.

J. C. Santamarina, Civil and Environmental Engineering, Georgia Institute of Technology, 790 Atlantic Dr. N.W., Atlanta, GA 30332-0355, USA.

H. Shin, Civil and Environmental Engineering, University of Ulsan, 23-409 Daehak-ro 93, Nam-gu, Ulsan, South Korea, 680-749. (shingeo@ulsan.ac.kr)